A New Technique to Infer Plasma Density, Flow Velocity, and Satellite Potential From Ion Currents Collected by a Segmented Langmuir Probe

Akinola Olowookere and Richard Marchand

***Abstract*— Compared with other types of Langmuir probes, segmented probes are arguably the least often used, to diagnose the state of plasma. With linear dimensions of the order of centimeters, these probes would induce perturbations, which would make them impractical in many laboratory plasma experiments. Their size, and the fact that they consist of several equipotential faces or "segments," from which individual currents are collected, introduces additional complexities in the construction of inference techniques for their characteristics. In this work, we focus on the use of spherical segmented probes mounted on a satellite and present new techniques to infer plasma (ion) densities, flow velocities, and satellite potentials, from currents collected by two segmented probes biased to two different fixed potentials relative to a spacecraft. This is done by carrying out 3-D kinetic self-consistent particle-in-cell (PIC) simulations to compute the response of a probe to space plasma under different environment conditions of relevance to satellites in low-Earth orbit (LEO) at low and mid-latitudes. Computed currents and the corresponding known plasma and satellite parameters used as input in the simulations are then used to create a solution library with which regression-based inference models are constructed, following standard machine learning techniques. The models trained with a subset of our synthetic dataset are found to yield excellent agreement with data in distinct validation sets. The models constructed with synthetic data are then applied to *in situ* measurements made with segmented Langmuir probes mounted on the Proba-2 satellite, and the inferences are compared with densities reported on the Proba-2 data portal. The advantage of our approach is that it readily produces uncertainty margins that are specifically related to the inference technique used.**

***Index Terms*— Kinetic simulations, regression techniques, space plasma, spherical segmented Langmuir probe.**

I. Introduction

THE interaction of spacecraft with ionospheric plasma causes perturbations, which affect the measurements made with particle sensors. Several studies are being done to better understand the physical properties of space and laboratory plasma using different instruments. For example, different flow meters have been used on satellites to determine the plasma direction of flow [1], [2]. IAP was flown on DEMETER to measure the direction of ion bulk velocity, in addition to their energy distribution and plasma (ion) density [2], [3]. Similarly, ion drift velocities can be determined with the thermal ion imager (TII) on Swarm [4]. In addition, VEIS on the WIND satellite and flowmeter on Dynamics Explorer B have been used in studying the plasma flow directions [5], [6], [7]. Mach probes have also been used to measure the plasma flow speed or Mach number. There are several types of Mach probes such as the parallel Mach probe which consists of two directional probes separated by an insulator [8]. Using the upstream and downstream ion saturation currents of the probes, the Mach number can be determined, from which the velocity is obtained using different theoretical approximations [8], [9], [10], [11]. Other types of Mach probes include the rotating Mach probe, the Gundestrup probe, and the vico-Mach probe, and their detailed operation can be found in the literature [8], [9], [12]. Another multipurpose Langmuir probe used to measure the plasma velocity is the spherical segmented Langmuir probe, first flown on DEMETER [13]. The probe is designed to leverage the angular anisotropy of the current collected by each of its six segments to determine the plasma bulk velocity [13]. This type of Langmuir probe was later implemented on the European Space Agency (ESA) micro satellite, Proba-2. It consists of seven equi-potential segments, or spherical caps and a guard holding them together [14]. Numerical modeling of the spherical segmented Langmuir probe has also been done using particle-in-cell (PIC) simulations to investigate the variations in the collected currents of each of the segments, and the results obtained are similar to what is reported for DEMETER [15], [16].

In the following, we apply kinetic simulations and regression techniques to construct the inference models for measurements made with a segmented probe. The goals are: 1) to characterize the response of each segment on the probe to different plasma velocities and environment conditions; 2) to construct regression models to infer plasma densities, transverse flow velocities, and satellite potentials of the satellite; and 3) to assess the skill of the inference models.

Manuscript received 11 April 2022; revised 18 July 2022 and 2 September 2022; accepted 3 September 2022. Date of publication 3 October 2022; date of current version 21 October 2022. This work was supported in part by the Natural Science and Engineering Research Council of Canada (NSERC) and in part by Compute Canada. The review of this article was arranged by Senior Editor S. T. Lai. *(Corresponding author: Akinola Olowookere.)*

The authors are with the Department of Physics, University of Alberta, Edmonton, AB T6G 2E1, Canada (e-mail: olowooke@ualberta.ca).

Color versions of one or more figures in this article are available at https://doi.org/10.1109/TPS.2022.3205868.

Digital Object Identifier 10.1109/TPS.2022.3205868

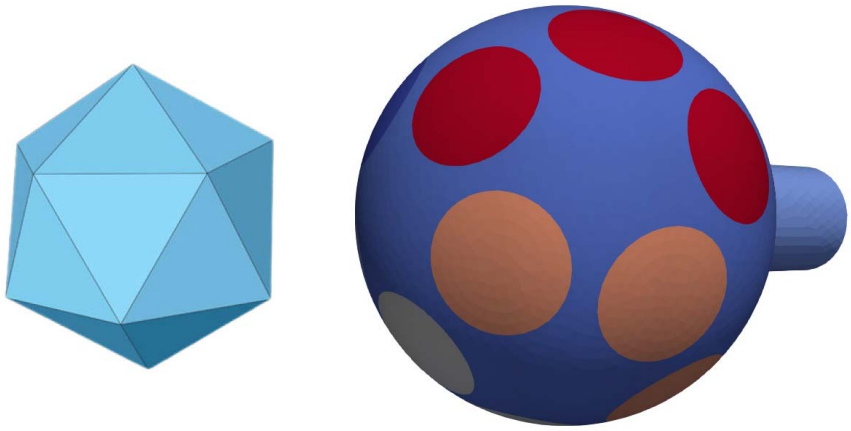

Fig. 1. Illustration of the geometry of the segmented probe used in the simulation (right) and an icosahedron (left).

We consider two geometries. The first one is for a sphere probe with 20 segments at the centers of the 20 triangles of a regular icosahedron. This idealized geometry is chosen for its symmetry, and it is used to make a first assessment of the regression method. The second geometry represents the actual Proba-2 spherical segmented probe. In both the cases, the equipotential post to which the probes are attached is included in the simulations. The synthetic datasets are constructed for both the geometries; a subset of which is used to train models, which can then be assessed by applying them to make inferences with a distinct subset used as the validation set. The models trained with synthetic data are then applied to the actual *in situ* current measurements obtained from the Proba-2 data portal, for the segmented probes [17]. Our model inferences are then compared with data available from the Proba-2 portal. In the remainder of this article, the approach used to create the two synthetic datasets is explained. The two machine learning techniques used to train our models are presented in Section II, while the inference model constructed using the two synthetic datasets and the validation results are presented in Section III. The trained models are then applied to the *in situ* measurements in Section IV, and the summary of our findings is presented in Section V.

II. Methodology

First, an idealized segmented Langmuir probe used in the simulations is constructed on a regular icosahedron with 20 triangular faces, 12 vertices, and 30 edges. The coordinates of the center of each triangular face are used as the centers of the 20 caps (segments) on the probe. The advantage in this idealized geometry is to leverage the fivefold symmetry of the structure and minimize the number of required simulations. Fig. 1 illustrates an icosahedron and the segmented probe used in the simulations, which consists of 20 5-mm radius segments on a 2-cm radius conducting guard and the 1.5-cm long, 6-mm radius cylindrical post holding them. In the simulations, the spherical guard, the 20 segments, and the cylindrical post are assumed to be equipotential, and the currents collected by these independent components are calculated separately. It is assumed that the probe is held by a boom sufficiently far from any other satellite components in the ram direction, so that the probe is not affected by any other component on the satellite. The segments on the probe are assembled into four groups of five segments at angles 37.38°, 79.19°, 100.81°, and 142.62° relative to the axis of the post, which we assume is the ram direction. The response of the probe to different plasma conditions is simulated with PTetra, a 3-D PIC code, and the simulation domain is discretized with an adaptive unstructured tetrahedral mesh [18]. The electrons and ions are treated kinetically, and the fields and particle trajectories are calculated self-consistently at every time step [15], [19], [20], [21]. The plasma parameters considered in the simulations are obtained from the International Reference Ionosphere (IRI) model for conditions encountered by satellites in low-Earth orbit (LEO) at latitudes in the range of 65S–65N, different longitudes, at altitudes ranging from 500 to 730 km, different seasons, and times of the day. The plasma (ion) densities considered vary from 9×10^{10} to 2×10^{12} m^{-3}, electron temperatures range from 0.05 to 0.25 eV, ion temperatures from 0.05 to 0.25 eV, and effective ion masses from 5 to 16 amu. A summary of the parameters used in the simulation is presented in Table I.

A. Construction of the Synthetic Dataset

The dataset used in this work is made from the simulation of an isolated spherical segmented Langmuir probe (see Fig. 1) held by a boom, in an otherwise uniform background plasma, without accounting for a satellite and other instruments. The probe voltages ranging from -5 to -1 V, relative to the background plasma, are considered so that the probe collects mostly ions. However, with the probe at -1 V, the probe might collect small amounts of electron currents in addition to the ion currents. In the simulations, we account for plasma with multiple ion species as presented in Table I, plasma flowing directly from the ram direction and at angle 18° from the ram direction, and ram speeds ranging from 7000 to 8000 m/s. Two sets of data are created. In the first case, a probe at fixed voltages ranging from -5 to -1 V relative to the background plasma is considered, independently of the floating potential

TABLE I

SIMULATION PARAMETERS USED IN THE CONSTRUCTION OF OUR SOLUTION LIBRARY

n 10^{10} m^{-3}	T_e eV	T_i eV	m_{eff} amu	n_{O^+} %	n_{H^+} %	n_{He^+} %	n_{N^+} %
18.73	0.2207	0.09438	12.62	97.87	1.76	0.11	0.27
12.04	0.2144	0.09356	15.83	94.73	0.00	0.11	5.16
15.11	0.1791	0.1006	15.88	95.59	0.00	0.05	4.36
6.476	0.2464	0.1089	15.93	99.73	0.00	0.15	0.12
84.19	0.09467	0.09467	14.19	94.79	0.78	0.13	4.29
8.169	0.09805	0.09805	11.01	96.57	2.95	0.37	0.11
22.90	0.1515	0.1003	15.86	95.07	0.00	0.06	4.88
6.446	0.07218	0.07218	6.27	86.39	10.20	0.62	2.79
4.579	0.1354	0.1202	9.29	94.68	4.72	0.48	0.12
4.572	0.1692	0.1102	12.80	98.02	1.61	0.27	0.09
1.160	0.1632	0.1203	8.23	92.97	6.19	0.53	0.31
2.540	0.1717	0.1123	12.09	97.58	2.09	0.32	0.00
112.0	0.0983	0.0868	15.89	95.07	0.00	0.00	4.93
106.0	0.0935	0.0869	15.89	95.07	0.00	0.00	4.93
44.50	0.0894	0.0766	15.86	94.65	0.00	0.05	5.30
4.840	0.0591	0.0591	16.00	100.0	0.00	0.00	0.00
0.911	0.2268	0.2268	5.21	76.80	13.60	0.60	9.00

TABLE II

EXAMPLE PROBE VOLTAGES WITH RESPECT TO BACKGROUND PLASMA, FOR A SPACECRAFT FLOATING POTENTIAL RANGING FROM -6 TO -3 V, ASSUMING PROBES WITH FIXED BIAS VOLTAGES OF $+1$ V AND $+2$ V

V_f(V)	V_1(V)	V_2(V)
-6	-5	-4
-5	-4	-3
-4	-3	-2
-3	-2	-1

of the satellite. This simplification is made so as to focus on the inferences of the ion density and plasma transverse flow velocity, without complications associated with variable satellite potentials. The second case considered is for probes biased to 1 and 2 V relative to the satellite and satellite potentials varying randomly in the range -6 to -3 V. The voltages of the probes relative to the background plasma are determined using the relation

$$V = V_f + V_b \tag{1}$$

where V_f is the satellite potential relative to the plasma, V_b is the probe bias voltage with respect to the spacecraft, and V is the probe voltage relative to the background plasma. Sample calculations of V are summarized in Table II. All the simulations are carried out to steady state, at which time the net currents collected by each segment, the guard, and the cylindrical post are computed. Test particle back-tracking simulations are then used to calculate the particle distribution functions at selected points on the sphere by applying Liouville's theorem in a collisionless plasma [22]. The electric fields used in the calculation of particle trajectories are obtained from the PIC simulations in which they are calculated self-consistently. The particle fluxes and current densities are then determined numerically from moments of the distribution functions discretized on an adaptive octree velocity grid [23], [24], [25]. The points at which the particle distribution functions are calculated are selected on the probe spherical surface along four meridians 90° apart in the plane perpendicular to the ram direction, and they are distributed symmetrically relative to the flow direction. The selected

TABLE III

LIST OF ANGLES θ RELATIVE TO THE RAM DIRECTION OF POINTS CONSIDERED IN EACH MERIDIAN

First Meridian	Second Meridian	Third Meridian	Fourth Meridian
0.0°	3.75°	7.5°	11.25°
15.0°	18.75°	22.5°	26.25°
30.0°	33.75°	37.5°	41.25°
45.0°	48.75°	52.5°	56.25°
60.0°	63.75°	67.5°	71.25°
75.0°	78.75°	82.5°	86.25°
90.0°	93.75°	97.5°	101.25°
105.0°	108.75°	112.5°	116.25°
120.0°	123.75°	127.5°	130.0°

points are located at different colatitudes θ relative to the ram direction in the range $0° \leq \theta \leq 130°$, as listed in Table III. After calculating the current densities, they are then fitted as a function of θ with a sum of cos functions as

$$I(\theta) = \sum_{k=0}^{N} a_k \cos(k\theta), k = 0, 1, \ldots, N \tag{2}$$

for each set of plasma parameters considered. In (2), a_k are the fitting coefficients, and N is the number of fitting coefficients. In practice, we find that $N = 6$ provides excellent accuracy, with maximum relative errors (MREs) not exceeding 1.2%. The fits are then used to calculate the currents collected by each segment on the probe for arbitrary plasma flow directions in the range [0°,15°] relative to the ram direction. The currents collected by segments are obtained using the fit to calculate the current density at the center of the triangles defining each segment. Note that with our unstructured tetrahedral mesh, the segments are delimited by triangles corresponding to faces of tetrahedra adjacent to the segments. Owing to the symmetry of the probe, the angle θ in the fit is simply the angle between the direction of the incoming plasma flow and the radial position of the triangle center in a given segment. The current collected by each segment is obtained by adding the current densities times the areas of the triangles in the segment. The performance of the fits is accessed by comparing the currents calculated directly from the PIC simulations, with the corresponding currents calculated using the fits as described above. The accuracy of the calculated currents is found to be within 3% in all the cases considered.

B. Machine Learning Approach

There are different methods used in the machine learning approaches to train the inference models, depending on the nature of the problem. In this work, we use two approaches based on: 1) radial basis functions (RBFs) and 2) deep learning neural networks (NNs). These are briefly explained below.

1) Radial Basis Functions: RBF is a relatively simple but efficient regression technique to construct the inference models for complex relationships between the output and input variables. It has been widely used for interpolating scattered data in a multidimensional space [26], [27], [28]. The implementation of RBF interpolation requires a set of points (nodes) called centers, a basis function (interpolating function), and the dataset to be interpolated. The technique

consists of inferring a dependent variable Y at position $\bar{X}$ in an n-tuple space of independent variables, with a linear superposition of a function of the distance between $\bar{X}$ and selected reference points or centers $\bar{X}_i$, as in

$$Y \simeq \sum_{j=1}^{N_p} a_j G\left(|\bar{X} - \bar{X}_j|\right) \tag{3}$$

where G is a suitable basis or interpolation function, a_j are the fitting coefficients, and N_p is the number of center points. The performance of this regression technique depends critically on the choice of the interpolating function G and centers $\bar{X}_i$ as explained in [29]. In our problem, $\bar{X}$ is a tuple consisting of currents collected by the segments on the probes, and Y represents the plasma parameter of interest to be inferred, which can also be a tuple or a scalar. To first approximation, the fitting parameters a_j are determined by requiring exact collocation at the centers; that is by solving equations

$$Y_i = \sum_{j=1}^{N_p} a_j G\left(|\bar{X}_i - \bar{X}_j|\right), \quad i = 1, 2, \ldots, N. \tag{4}$$

There are different methods used to select a set of centers. One way is by carrying out an extensive search for the set of N_p centers which minimizes the cost function among all the possible combinations of N_p centers chosen from $\mathcal{N}$ nodes in the entire dataset. The computation time of going through all the possible combinations can be prohibitively long if the model is trained using a large dataset, and the time increases rapidly with an increase in the number of centers. The strategy used in this work in selecting N_p centers consists of successively and randomly selecting M small subsets of nodes from the full training set, each containing $\mathcal{M}$ nodes ($\mathcal{M}$ being the batch size). For the first batch, we consider all the possible combinations of N_p centers among the $\mathcal{M}$ nodes, and the set of centers that minimizes the cost function, calculated on the full training set, is temporarily kept as optimal. These N_p nodes are then kept in the next batch, in which $\mathcal{M} - N_p$ randomly selected nodes are selected from the full $\mathcal{N}$ training set. This random selection must of course be made so as not to duplicate the previously found optimal N_P nodes. These steps continue until the M number of batches have been considered, and the final set of centers that minimizes the cost function is selected for the final model [30].

2) Neural Networks: NNs have become a useful tool in modern scientific research, in space physics, as well as in many areas of science, medicine, and other fields [31], [32], [33], [34]. In this work, we use a multilayer perceptron (MLP) network, which is one of the commonly used network architectures in training NN models [35]. The network is arranged in a layered feedforward topology as shown in Fig. 2. The weighted sums of the input data from the input layer are passed through a nonlinear activation function which produces an output which is then passed to the next layer as the input data. This continues until the final output is produced in the output layer. For illustration, given nodes j in layer i with values z_{ij}, the nodes in the next layer $i + 1$ take in the output of each node in the previous layer, and the value is assigned $z_{i+1,k}$ as in

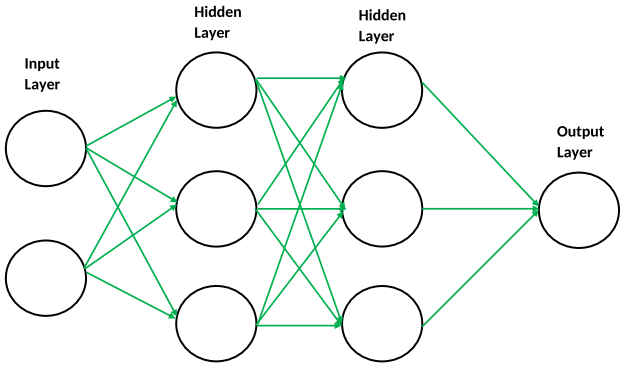

Fig. 2. Illustration of a feedforward NN.

$$z_{i+1,k} = \sum_{j=1}^{n_i} w_{i,j,k} f\left(z_{i,j} + b_{i,j}\right) \tag{5}$$

where n_i is the number of nodes in layer i, $w_{i,j,k}$ are the weights, and $b_{i,j}$ are the bias terms. The weights and bias terms are optimized using a back-propagation learning scheme using algorithms such as gradient descent, ADAgrad, RMSprop, or ADAM [36], [37]. Each node in the input layer is assigned a current from one of the segments, and all the models are trained with TensorFlow [38]. The bias terms in (5) are all set to zero when training the model because they are found to make no significant difference in the outcome, and the activation function used is the rectified linear unit (ReLU); $f(z) = \text{ReLU}(z) = \max\{0, z\}$ which performs a nonlinear combination of all the input data. Another key component in NNs is the cost function, which measures the discrepancy between the inference and known data.

III. Construction of Inference Models

The inference models are constructed using synthetic datasets generated for the idealized segmented probe and the Proba-2 probe. The models' skill is then assessed in each case by comparing inferences to known the values used as input in the simulations. Comparisons between the inferences and data from the validation sets are presented below.

A. Idealized Probe Geometry

As a first step, the currents collected by the ten segments located on the side of the probe facing the ram direction are calculated as described in Section II-A. For simplicity, in this first assessment, the probe is assumed to be at a fixed potential ranging from -5 to -1 V in steps of $+1$ V relative to the surrounding plasma. We create a dataset consisting of 24 000 nodes, each with ten tuples of currents for each of the ten segments, followed by the physical parameters to be inferred; that is, the transverse velocity with magnitudes ranging from -1000 to 1000 m/s, and the densities are listed in Table I. Having generated the synthetic data, we randomly split the dataset into two disjoint subsets; one being used to train the inference models, and the other for assessing the accuracy

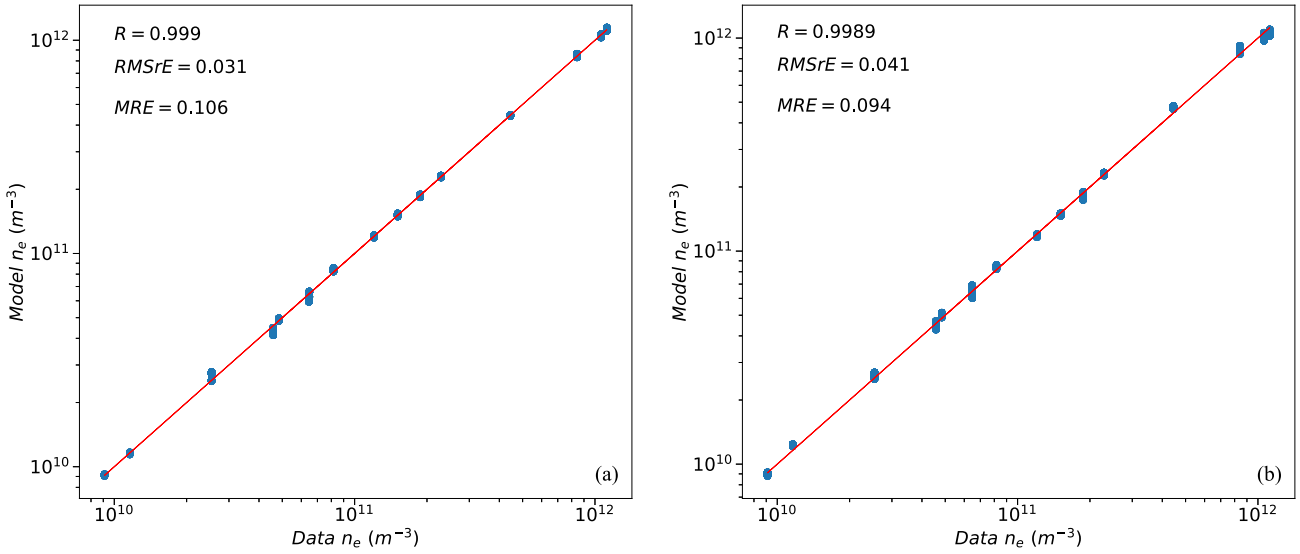

Fig. 3. Comparison between inferred densities using (a) NN and (b) RBF with six centers and actual densities in the idealized probe validation dataset. The straight line corresponds to a perfect correlation between the two densities.

of our inferences. Our training set consists of 14 500 randomly selected nodes from the solution library, while the validation set consists of the remaining 9500 nodes. Using the two regression techniques explained in Section II-B, the models are trained to infer the ion density n_i and plasma transverse velocity. Each model is then assessed for accuracy by comparing its inferences with known values in the validation set.

1) Density Model: Both the NN and RBF models are used to infer the plasma (ion) density. The NN consists of an input layer of ten nodes for each of the ten currents, two hidden layers of eight and five nodes, respectively, and a single output node for the density. The cost function used is the mean absolute relative error (MARE) given by

$$\text{MARE} = \frac{1}{n}\sum_{j=1}^{n}\left|\frac{\text{Y}_{\text{dt}} - \text{Y}_{\text{inf}}}{\text{Y}_{\text{inf}}}\right| \tag{6}$$

where n is the number of entries in the training dataset, Y_{dt} is the data value, and Y_{inf} is the inferred value. The cost function is minimized with the Adam algorithm, which is an adaptive optimization algorithm implemented in Tensor Flow [39]. This algorithm was chosen among other minimization options because of its optimal performance in our problems. The correlation plot in Fig. 3(a) shows a comparison between the NN inferences and data from the validation set. The model skill is assessed with the MRE, the root mean square relative error (RMSrE), and the Pearson correlation coefficient (R). The model inferences are in excellent qualitative and quantitative agreement with the validation values, with an MRE not exceeding 11% and RMSrE of 3.1%. In the RBF model, 50 batches, each consisting of 90 randomly selected nodes from the training set, are used. Six center points are used in the model, as this number is found to provide a good balance between training and validation, while avoiding overfitting. The cost function used in constructing the RBF model is the MRE. Several interpolating functions were tested, but the best one that minimized the MRE for the density model is $G = |I - I_j|^{1.8}$. Fig. 3(b) shows a correlation plot of the inferred density as a function of the actual densities from the validation set. The skill of the RBF model is assessed using the same metrics as for the NN model and it shows a comparable inference accuracy between the two models with the RBF models having lower MRE in contrast to RMSrE which is higher in RBF than the NN model. The correlation plots for both the methods also show that model predictions closely follow the ideal correlation line, with a strong affinity as measured with the Pearson correlation coefficients which are close to unity in both the cases.

2) Transverse Velocity Inferences: Here, only the NN model is applied to infer transverse velocities, because in this case, RBF was found to produce lower quality results. The NN used has five layers, comprising the input layer with ten nodes, three hidden layers with eight, six, and four nodes, respectively, and an output layer with two nodes for the components of the transverse velocities. The cost function used is the mean square error defined in (7). Fig. 4 shows a 2-D scatter plot of the components of the transverse velocities, with the color bar showing the absolute errors in the model inferences. The plot is dominated by blue points, with very few red and light red points which indicates that most of the errors in the model inferences fall below 100 m/s. The maximum absolute error (MaxAE) in the inferences is 193.54 m/s, but almost 98% of the values inferred have an absolute error less than 100 m/s as seen in the histogram in Fig. 5, showing the errors' distribution. The mean absolute error (MeanAE) is 28.93 m/s and the root mean square error (RMSE) is 45.41 m/s, which corresponds to 2.3% relative to the range of speeds, $[-1000, 1000\ \text{m/s}]$ considered in the simulation. The values of these errors show a good quantitative agreement between the model inferences and the known transverse velocities used as input in the simulation

$$\text{MSE} = \frac{1}{n}\sum_{j=1}^{n}(|\text{Y}_{\text{dt}} - \text{Y}_{\text{inf}}|)^2. \tag{7}$$

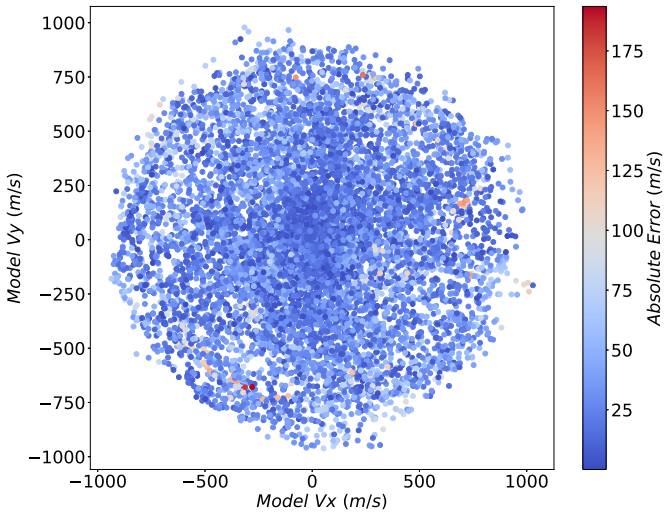

Fig. 4. Inferred transverse velocities in the range of −1000 to 1000 m/s using the NN model for the idealized probe. The color scale shows the absolute errors in the velocity model inference.

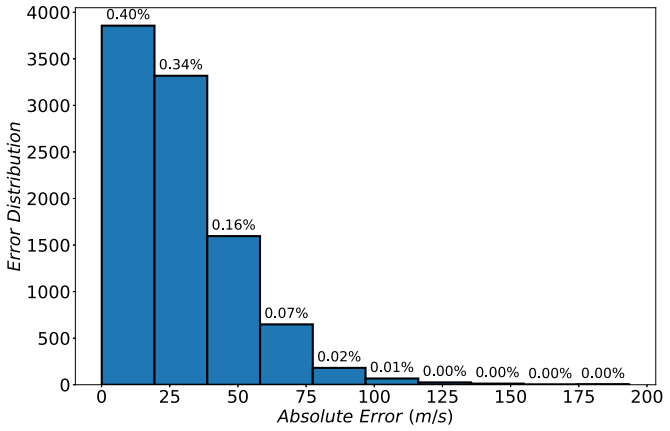

Fig. 5. Histogram showing the distribution of the absolute error in the velocity inference model for the idealized probe.

B. Proba-2 Probe Geometry

The synthetic data used in this part are generated for the segmented Langmuir probe A (SLPA) geometry, as one of the Proba-2 dual segmented Langmuir probe (DSLP). DSLP is part of the scientific payload of the ESA micro satellite Proba-2, which was launched on November 2, 2009 [40]. It consists of two identical segmented Langmuir probes, SLPA and SLPB, with each having eight equipotential independent collectors electrically insulated from each other. The collectors comprise seven circular segments with a radius of 5 mm and a guard electrode of radius 2 cm holding the segments. The segments are positioned around the sphere at different locations. In the Proba-2 data portal, the ram velocity of the satellite is stated to be in the $-Y$-direction in the spacecraft body reference frame (BOF), and thus the plasma flow velocity in the spacecraft frame is assumed to be in the $+Y$-direction. The segments on SLPA are positioned relative to the segments' frame of reference (SEG), which is different from the spacecraft BOF. The BOF can be transformed to the SEG

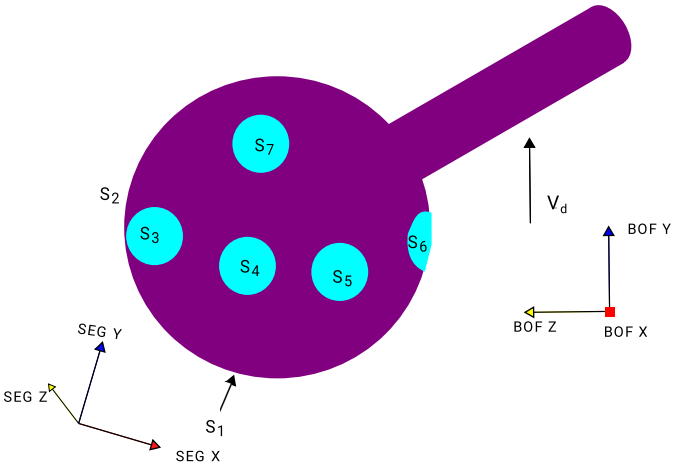

Fig. 6. Illustration of the position of the segments relative to the direction of plasma flow. V_d represents the plasma flow velocity in the probe frame.

by first performing a counterclockwise rotation around the BOF x-axis by 40°, followed by another counterclockwise rotation of 60° around the z-axis. This transformation is necessary because the fit in (2) is done relative to a system in which the z-axis coincides with the cylindrical post axis. After transformation, the trigonometric fit is used to determine the current density at the center of the triangles defining each of the seven segments on the probe, which makes it possible to integrate, and determine the current collected by each segment as described in Section II-A. The currents are calculated by assuming that the probe is biased at a fixed voltage relative to the satellite. The advantage of considering a fixed bias probe is that measurements can be made with higher temporal and spatial (owing to the large satellite speed) resolutions. The satellite potentials considered in creating the synthetic dataset, used to train models, range from −6 to −3 V. This choice is based on the reported probe's characteristic on the Proba-2 SLPA portal, and different transverse speeds in the range [−1000, 1000 m/s] are also considered. A total of 8500 nodes are generated in our solution library, each entry consisting of the currents calculated for each segment, followed by the densities, the transverse velocities, and the satellite potentials. Here again, the dataset is randomly divided into a set consisting of 5950 nodes used to train the models and a distinct set containing the remaining 2550 nodes used for validation. The models are trained using currents for all the segments excluding only segment 6 (see Fig. 6). The choice of the six segments among the seven on the sphere is dictated by the orientation of the probe on Proba-2 (see Fig. 6) and the limited interval in angle ($0° \leq \theta \leq 130°$) for the fitted current densities, relative to the ram direction. With currents from the probes, our independent variables then consist of 12 tuples, six from a probe biased at 1 V and six for a probe biased at 2 V.

1) Density Model Assessment With Synthetic Data: The density inference models are constructed using an NN and RBF. The NN consists of five layers, which comprise the input layer with 12 nodes each for the currents collected by the selected six segments at the two biased voltages, three hidden layers with ten, seven, and three nodes, respectively,

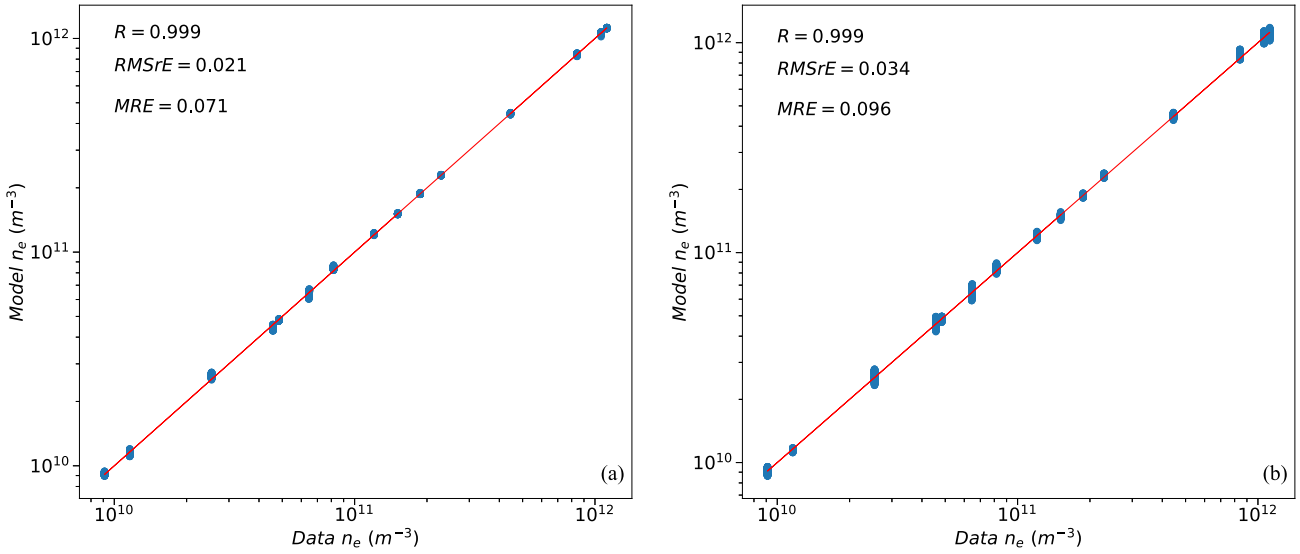

Fig. 7. Inferred densities against validation dataset densities for the Proba-2 synthetic data, using (a) NN inferences and (b) RBF-inferred densities with six centers. The line corresponds to a perfect correlation between the two densities.

and an output layer with a single node. The model is trained using the mean absolute percentage error given in (6) as a cost function. This is minimized to achieve an optimal model, using the same activation function as in Section III-A1. In the RBF model, six centers are used, the interpolating function chosen is again $G = |I-I_j|^{1.8}$, and the model is constructed by minimizing MRE. Fig. 7 shows the correlation plots obtained when comparing model inferences when the trained models are applied to the validation set. Both the techniques show excellent agreement with known data, with the NN slightly outperforming RBF with an MRE of 7.1% and RMSrE of 2.1% compared with MRE of 9.6% and RMSrE of 3.4% for RBF. The points on the plot for both the methods closely follow the perfect correlation line, but the vertical spread in the RBF model is slightly larger than that obtained with NN. The Pearson correlation coefficient R values indicate the two models have an excellent affinity with known density values from our validation set.

2) Satellite Potential Model Assessment With Synthetic Data: Here, we only consider results obtained with an NN to infer the satellite potential, because its inference skills are significantly better than those found with RBF. The NN model has the same structure as the one used in training the density model presented in Section III-B1. In this case, however, instead of using the mean absolute percentage error given in (6) as the cost function, we used the mean square error, with which we achieved the best inferences. The skill of the trained model is assessed using different metrics when applied to the validation dataset. The Pearson correlation coefficient between the inferred satellite potential and the actual satellite potential is 0.995, which indicates a strong affinity. A correlation plot between these values is shown in Fig. 8, with the calculated values of MaxAE, RMSE, and MeanAE. From the plot, we note a slight extrapolation in the model inferences, as a small fraction of the points fall outside the range in the data used to train the model. Quantitatively, the overall performance of the model is good, with a MeanAE of 0.063 V which corresponds to 2.1% discrepancy relative to the range of satellite potential in the dataset.

3) Transverse Velocity Model Assessment With Synthetic Data: Here also, only the NN approach is used to construct a model for the transverse velocity, because it produces better model inferences than RBF. In this case, the network has five layers, with the input layer having 12 nodes and the three hidden layers consisting of 15, nine, and six nodes, respectively, while the output layer consists of two nodes, for the two components of the transverse velocity. The model is obtained by minimizing the mean square error defined in (7). Fig. 9 is a scatter plot of the components of the transverse velocities, with the color bar showing the absolute errors in the model inferences. In the figure, most points are blue, indicating that the majority of the absolute errors in the inferences fall below the 100-m/s mark. This observation is confirmed with the histogram in Fig. 10, showing the distribution of inference errors when applying the model to the validation set. The histogram shows that nearly 99% of the inferences are made with absolute errors not exceeding 100 m/s. The skill of the model is further quantified with the MeanAE and the RMSE, with values 22.54 and 39.53 m/s corresponding, respectively, to errors of 1.12% and 1.98% relative to the range [−1000, 1000 m/s] of transverse velocities in the dataset. These metric scores indicate an excellent model inference skill.

IV. Application to Proba-2 *In Situ* Measurements

In this section, we apply the models constructed in Section III-B to the Proba-2 SLPA measurements reported on the Proba-2 portal [17] on February 1, 2015 when the probe's voltage was swept between −7.62 and +7.62 V. These data archived in cdf format are downloaded from the Proba-2 data portal and converted into CSV format using the pycdf module imported from spacepy Python library. The I–V characteristics and the derived data are then obtained from

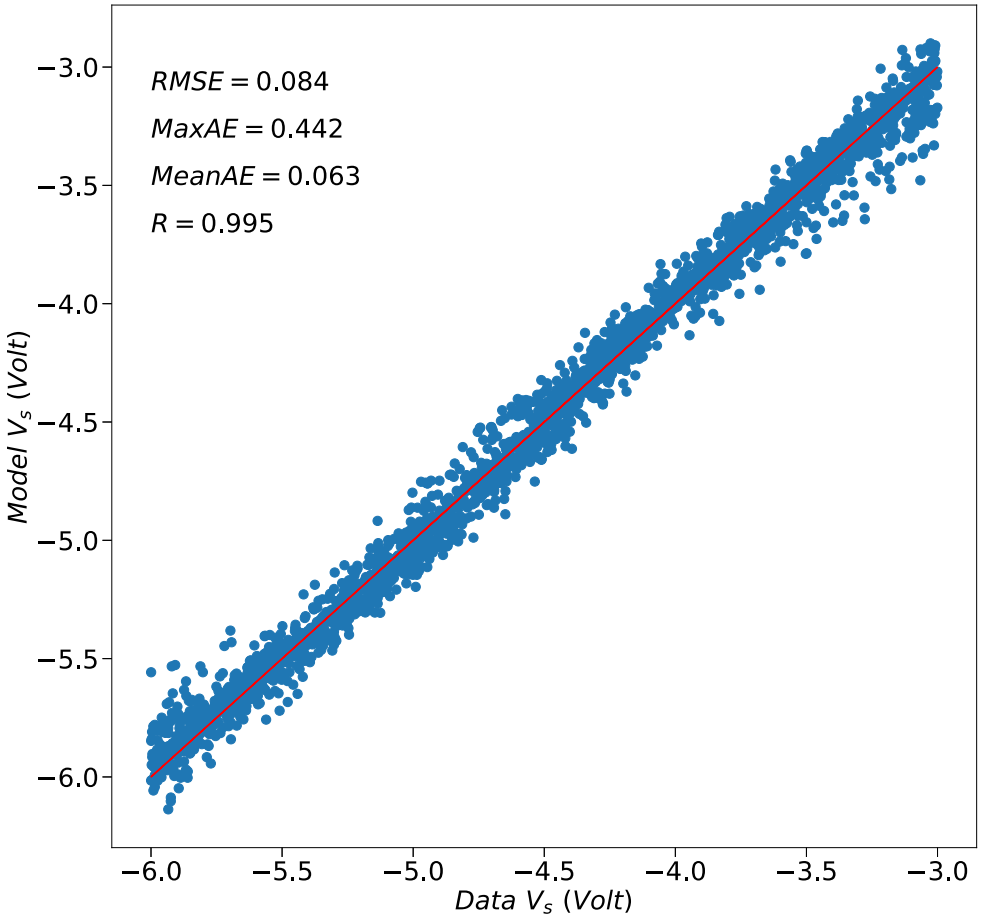

Fig. 8. Comparison between satellite potentials inferred using the NN model and actual potentials in the synthetic dataset constructed with the Proba-2 geometry. The line corresponds to a perfect correlation between the two potentials.

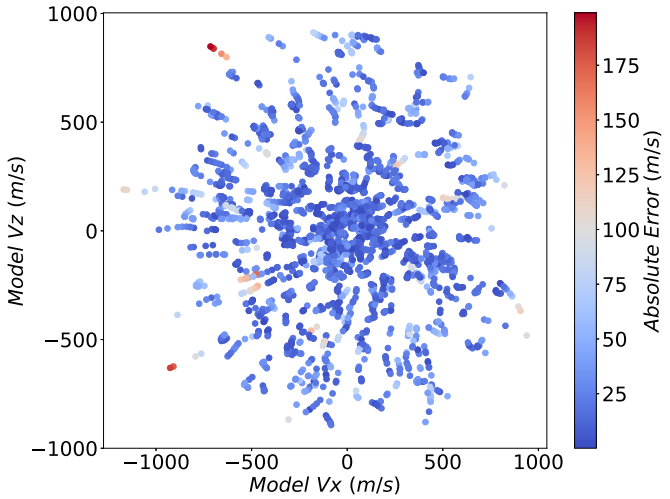

Fig. 9. Inferred transverse velocities in the range of −1000 to 1000 m/s using the NN model and actual velocities in the synthetic dataset constructed with the Proba-2 geometry. The color scale shows the absolute errors in the velocity model inference.

the CSV formatted files. The currents used are obtained from the measured I–V characteristics for each of the segments and the guard when the probe is operated in sweep mode between −7.62 and +7.62 V. In addition to the probe's I–V characteristics, the portal also reports electron densities and floating potentials inferred from each segment separately, as well as from the spherical guard. The reported data on the portal have a quality flag of 1 or 0, indicating good or low quality, respectively. Only data with a quality flag of 1 are used in our analysis. Another point worth noting is that electron densities and floating potentials reported for these probe components are generally all different from one another, and to the authors' knowledge, the method used to infer these reported values is not documented. Owing to the lack of information concerning the method used to infer the physical parameters reported on the Proba-2 data portal, and unknown uncertainties in these parameters, it is not possible to assess the accuracy of our inferences, based on quantitative comparisons with the reported values and to conclude which, between our inferences, or those reported on the portal, are likely the most accurate. In this section, we use the same models presented in Section III-B, trained using synthetic data generated assuming probe biased at fixed voltages of 1 and 2 V. The assumption of fixed bias probes is of course different from the sweep mode actually used with these probes. The measured currents needed in our model as the independent variables are nonetheless obtained by fitting each segment

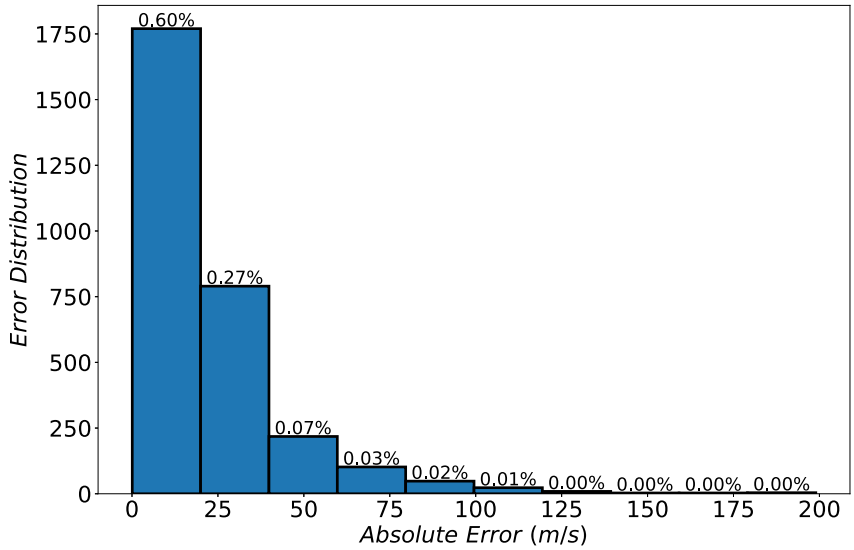

Fig. 10. Histogram of the distribution of the absolute errors in the velocity inference model when applied to the synthetic dataset constructed with the Proba-2 geometry.

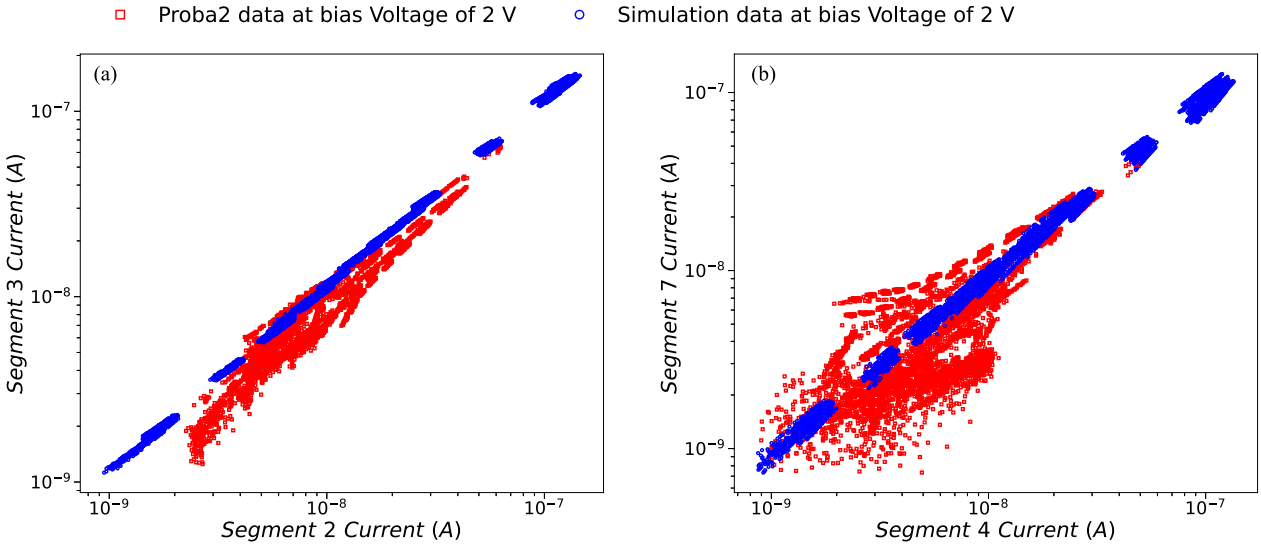

Fig. 11. Correlation plots for pairs of currents collected by (a) segments 2 and 3 and (b) segments 4 and 7. The blue circles are taken from our synthetic dataset, while the red squares are from Proba-2 measurements reported for February 1, 2015 on the portal [17].

characteristic of one of the Proba-2 segmented probes in the range −1.5 to 2.5 V, and using these fits to interpolate the current collected at 1- and 2-V bias voltages. As a first test, and to assess whether the currents found in the simulations are of relevance to the measured currents, we show in Fig. 11 samples of correlation plots between simulated and measured currents collected by segments 2 and 3 [see Fig. 11(a)] and segments 4 and 7 [see Fig. 11(b)].

The red squares are from Proba-2 SLPA measurements, and the blue circles are from the simulations. This comparison is also useful to eliminate cases corresponding to currents not considered in the synthetic dataset, which if included would require our models to extrapolate beyond the range of parameter space in which they were trained. The figure shows an overlap between the range of the *in situ* currents and the synthetic data currents, with the synthetic data currents extending further to the right (higher currents) than the experimental data. These higher values in the synthetic data currents are likely due to the fact that we consider plasma (ion) densities in the order of 10^{12} m^{-3} in the simulations, which are more than the range of the reported densities in the Proba-2 portal. In addition, a wider spread is noted in the experimental data at low currents compared with the simulated currents, which might be due to enhanced relative noise in these lower currents.

The NN model is then applied to infer the plasma (ion) density using the measured currents as the input. The NN model is used here rather than RBF, because it proved to be more accurate based on the validations made with the synthetic data. The average values for each set of the electron

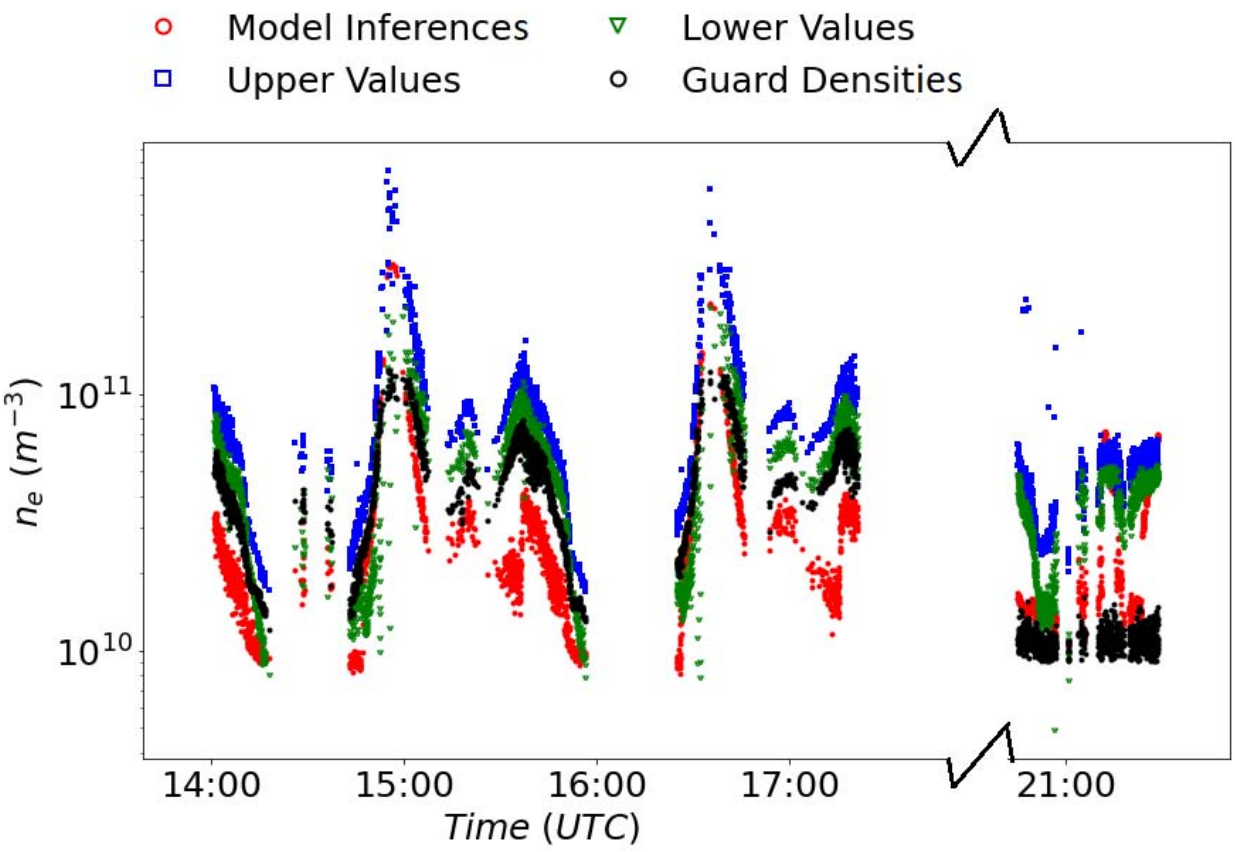

Fig. 12. Comparison between densities inferred using the NN model (red circles), with those reported for the guard (black circles), the upper (blue squares), and lower (green inverted triangles) density boundaries of the confidence interval. The confidence interval is calculated from the averages and standard deviations of densities reported on the Proba-2 portal for the six segments considered. The gaps in the comparison correspond to currents outside the range over which our models were trained.

densities reported for the six segments considered and their respective standard deviations are calculated. Using these two values, we determine a confidence interval delimited by the upper and lower boundaries for each electron density by adding and subtracting the standard deviations to the average. A comparison between our inferred ion densities with the guard reported electron densities and the calculated upper and lower boundary electron densities is shown in Fig. 12. This comparison is done based on the quasi-neutrality of plasma, that is, with an assumption that the ion density and electron density are equal. The comparison shows general qualitative agreement between our inferred densities and those reported in the Proba-2 portal, albeit with the reported density being larger than NN-inferred density by more than 100%. The inferred densities are more consistent with the reported guard densities, than with those calculated for the segments, and both are generally below these intervals. The gaps or jumps in the horizontal axis scale in the plots are due to the removal of data outside the range of the simulated current used to construct the model or data with quality flag of zero. The correlation plots between the inferred densities and *in situ* reported densities are shown in Fig. 13, for each of the segments and the guard when using the NN model, with their respective RMSrE and MRE skill metrics. The model-inferred densities from the segments show significant scatter, mostly below the ideal correlation line, with inferred values lower than the ones reported by a factor ranging from 2 to 4. With the guard, excluding the lower and upper ends of the correlation curve, the inferred densities show noticeably less scatter, with values approximately 50% lower than those reported. The outlier, higher inferred densities corresponding to the lower ($\sim 10^{10}$ m^{-3}) and higher ($\gtrsim 10^{11}$ m^{-3}), also visible in Fig. 12 could be attributed for example, to sheath effects in regions of low-density (longer Debye lengths), photoelectron emission, which would

TABLE IV
SUMMARY OF THE METRICS OF SIMILARITY BETWEEN NN AND RBF INFERENCES, AND REPORTED INFERENCES OF THE DENSITIES FOR THE SIX SEGMENTS CONSIDERED

Segment	Method	RMSrE	MRE	R	offset
1	RBF	3.21	10.26	0.64	2.65
	NN	2.19	8.22	0.66	1.87
2	RBF	2.61	9.57	0.64	2.14
	NN	1.83	8.36	0.65	1.51
3	RBF	2.29	8.91	0.59	1.86
	NN	1.60	6.77	0.61	1.31
4	RBF	2.28	15.03	0.61	1.81
	NN	1.59	19.52	0.62	1.26
5	RBF	2.50	9.62	0.60	1.97
	NN	1.71	7.53	0.62	1.37
7	RBF	2.79	32.89	0.56	2.00
	NN	2.04	25.51	0.58	1.42

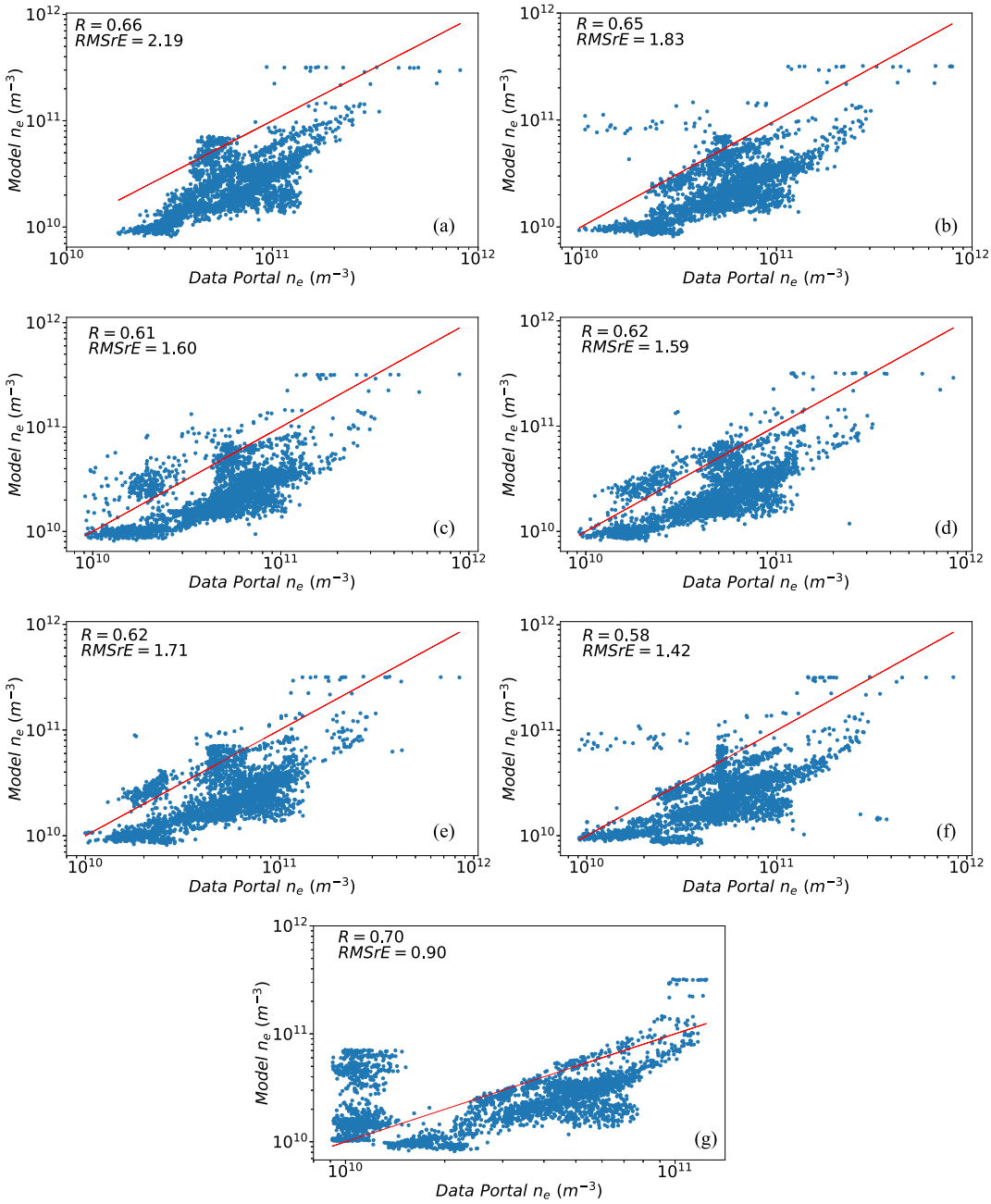

Fig. 13. Correlation plot of density inferences using the NN model and reported density on the Proba-2 portal for SLPA (a) segment 1, (b) segment 2, (c) segment 3, (d) segment 4, (e) segment 5, (f) segment 7, and (g) guard. The solid line corresponds to perfect correlation.

effectively result in enhanced ion collection, or nonthermal plasma in the polar regions. It is unfortunately not possible to go beyond mentioning these possibilities, considering that the latitudes and the zenith solar angles are not available from the data portal. In general, the inferences from the NN model are in good qualitative agreement with the reported electron densities and are closer to the *in situ* measurements than those obtained with the RBF model, as apparent with the similarity metrics listed in Table IV. The offset in the table is defined as the mean value of the relative errors in the inferred densities.

Finally, the satellite potential model and the transverse velocity model were also applied to the *in situ* measurement, but the inferences in these cases are far beyond the range of satellite potentials and velocities considered in training the models which indicates that these models in their present form are not applicable, possibly because of the proximity of the probes to the solar panels on Proba-2, not accounted for in the simulations.

V. Summary and Conclusion

Results are presented for the interpretation of measurements made by a spherical segmented Langmuir probe using two multivariate regression techniques. As a first step, the approach is assessed by considering an idealized probe consisting of

20 equipotential segments that are insulated from one another, from which ten segments are used in the analysis. The segments are positioned at different points on the spherical guard in such a way that they are symmetrically oriented relative to the direction of the incoming plasma flow. 3-D kinetic PIC and test particle simulations are made to calculate the currents collected by each segment at five fixed potentials relative to the background plasma for different plasma parameters relevant to the space environment near satellites in LEO at mid-latitudes. These currents and the corresponding plasma conditions are used to construct a first synthetic dataset to train inference models and assess their skills. In the simulations, only the spherical guard of the probe, its equipotential segments, and post are considered, which should be valid provided that the probe be on the ram side, sufficiently far from other satellite components. The geomagnetic field is also neglected, since the probe is biased so as to collect ion current, and the fact that for the conditions considered, ion gyro-radii in the ionosphere are of the order 1 m for H^+ and 5 m for O^+, which are much larger than the probe radius. In addition, by not accounting for the geomagnetic field, we also neglect the motional electric field $-\vec{v} \times \vec{B}$ in the satellite frame, which would result in additional potential differences ranging from $\sim$0 V at the equator, to $\sim$0.24 V at the poles, between the two probes, given the $\sim$90 cm separating them. The neglect of this potential offset is actually justified in our analysis, because, as mentioned in Section IV, the two probes on Proba-2 are not operated in the fixed bias mode, and the collected currents considered in our analysis are obtained by interpolation of a single probe characteristic at $+1$ and $+2$ V. The synthetic data are then used to construct the inference models for the plasma (ion) density and plasma transverse flow velocity. The density model is constructed using RBF and NN. RBF performs slightly better than NN based on the metrics used to quantify the models skill, both having MRE of 9.4% and 10.6%, respectively. A transverse velocity model is also trained using NN and it shows a good inference skill when assessed quantitatively using the synthetic validation dataset. The RMSE in the model inference is estimated to be 45.4 m/s, which is about 2.3% relative to the $[-1000, 1000]$ m/s velocity range, in arbitrary directions, considered in the dataset.

A second synthetic dataset is constructed using the Proba-2 probe geometry. The currents collected by the segments are calculated with a similar approach to that for the idealized probe, with the main difference being that variable effective satellite potentials relative to which the probes are biased, are assumed in the interval -6 to -3 V. The choice of the range of satellite potentials is based on the reported probe characteristics on the Proba-2 SLPA data portal. As with the idealized probe synthetic data, the RBF and NN models are trained to infer the plasma (ion) density. The two models yield densities with an MRE of 9.6% and 7.1% for RBF and NN, respectively. In this case again, the two models are found to be comparable in accuracy with NN inferences being slightly more accurate. The RBF-inferred densities obtained from the Proba-2 validation synthetic data when the satellite potential varies have comparable accuracy to the ones obtained with the idealized probe synthetic dataset when inferences are made with potentials relative the background plasma. With NN, the inferred densities are comparable but slightly more accurate when variable satellite potentials and fixed probe bias voltages are assumed, than in the idealized case with varying probe voltages relative to the background plasma. The overall performances of the models are good nonetheless in both the cases. The NN model is also trained to infer the satellite potential using the synthetic data. The model performance on the validation set is excellent, with a MeanAE of 0.06 V, which corresponds to an uncertainty around 2% relative to the range of satellite potential considered in constructing the model. The final model is constructed using the NN model to infer the transverse velocity, and the model has an excellent inference skill when applied to the validation dataset, with an RMSE of 39.5 m/s. The density models trained using the Proba-2 geometry synthetic data are then applied to the Proba-2 SLPA *in situ* measurement using the currents reported in the portal as the input values, and the models' inferences are compared with the reported values on Proba-2 portal. Systematic discrepancies are found in the inferred densities, with the reported data in the portal having higher values than the model inferences.

To conclude, kinetic simulations combined with multivariate regressions and machine learning techniques appear as a new promising avenue to better infer plasma parameters from currents collected with segmented Langmuir probes for which no analytic expressions are available. The simulations used here can reproduce known analytic results under conditions where they are valid. They can also account for conditions and physical processes and geometries which are too complex to be tractable analytically. The assessment of the two methods considered, using synthetic data, shows good inference skills for all the parameters considered, and the application of the density model to the actual *in situ* measurements is found to be in good qualitative agreement with the reported inferences on Proba-2. Quantitatively however, systematic differences are found, with regression-inferred densities being lower than the values reported on the data portal, generally by more than a factor 2. Considering the large discrepancies between densities reported for the Proba-2 seven segments and the spherical guard, and the lack of documentation concerning the method used to infer these densities, it is unfortunately impossible to assign confidence intervals to any of these densities and ascertain which of them is the most accurate. We can nonetheless report qualitative consistency between these densities and the ones inferred with our regression approach, which we see as promising, and hope that this preliminary success will motivate more experimental and simulation works aimed at designing better inference techniques for space plasma parameter from segmented Langmuir probes.

REFERENCES

[1] H. S. Bridge *et al.*, "The plasma experiment on the 1977 voyager mission," *Space Sci. Rev.*, vol. 21, no. 3, pp. 259–287, Dec. 1977.

[2] J. J. Berthelier *et al.*, "IAP, the thermal plasma analyzer on DEMETER," *Planet. Space Sci.*, vol. 54, no. 5, pp. 487–501, Apr. 2006.

[3] A. K. Sharma, A. V. Patil, R. N. Haridas, and M. Parrot, "Detection of ionospheric perturbations associated with earthquake using data of IAP and ISL instruments of DEMETER satellite," in *Proc. XXX URSI Gen. Assem. Sci. Symp.*, Aug. 2011, pp. 1–4.

[4] D. J. Knudsen *et al.*, "Thermal ion imagers and Langmuir probes in the swarm electric field instruments," *J. Geophys. Res., Space Phys.*, vol. 122, no. 2, pp. 2655–2673, 2016.
[5] J. Burch *et al.*, "IMF B_y-dependent plasma flow and birkeland currents in the dayside magnetosphere: 1. Dynamics explorer observations," *J. Geophys. Res., Space Phys.*, vol. 90, no. 2, pp. 1577–1593, 1985.
[6] R. Heelis and W. Coley, "East-west ion drifts at mid-latitudes observed by dynamics explorer 2," *J. Geophys. Res., Space Phys.*, vol. 97, no. A12, pp. 19461–19469, 1992.
[7] M. Adrian, A. Viñas, P. Moya, and D. Wendel, "Solar wind magnetic fluctuations and electron non-thermal temperature anisotropy: Survey of WIND-SWE-VEIS observations," *Astrophys. J.*, vol. 833, no. 1, p. 49, 2016.
[8] K.-S. Chung, "Mach probes," *Plasma Sources Sci. Technol.*, vol. 21, no. 6, Dec. 2012, Art. no. 063001.
[9] K.-S. Chung, S.-H. Hong, and K.-H. Chung, "Measurements of plasma flow velocity in DC plasma jets using perpendicular and parallel Mach probes," *Jpn. J. Appl. Phys.*, vol. 34, no. 8R, p. 4217, 1995.
[10] Y. Amagishi and T. Miyazaki, "Plasma flow measurements with Mach probe," *J. Phys. Soc. Jpn.*, vol. 67, no. 11, pp. 3774–3778, Nov. 1998.
[11] Y.-S. Choi, H.-J. Woo, K.-S. Chung, M.-J. Lee, D. Zimmerman, and R. McWilliams, "Determination of plasma flow velocity by Mach probe and triple probe with correction by laser-induced fluorescence in unmagnetized plasmas," *Jpn. J. Appl. Phys.*, vol. 45, no. 7R, p. 5945, 2006.
[12] C. S. MacLatchy, C. Boucher, D. A. Poirier, and J. Gunn, "Gundestrup: A Langmuir/Mach probe array for measuring flows in the scrape-off layer of TdeV," *Rev. Sci. Instrum.*, vol. 63, no. 8, pp. 3923–3929, Aug. 1992.
[13] J. P. Lebreton *et al.*, "The ISL Langmuir probe experiment processing onboard DEMETER: Scientific objectives, description and first results," *Planet. Space Sci.*, vol. 54, no. 5, pp. 472–486, Apr. 2006.
[14] P. Travnicek *et al.*, "The DSLP Langmuir probe experiment on-board PROBA2: Scientific objectives and description," in *Proc. EGU Gen. Assem. Conf. Abstr.*, 2009, p. 11967.
[15] E. Séran, J.-J. Berthelier, F. Z. Saouri, and J.-P. Lebreton, "The spherical segmented Langmuir probe in a flowing thermal plasma: Numerical model of the current collection," *Ann. Geophys.*, vol. 23, no. 5, pp. 1723–1733, 2005.
[16] N. Imtiaz, R. Marchand, and J.-P. Lebreton, "Modeling of current characteristics of segmented Langmuir probe on DEMETER," *Phys. Plasmas*, vol. 20, no. 5, May 2013, Art. no. 052903.
[17] European Space Agency. *Proba-2 Science Archive*. [Online]. Available: http://p2sa.esac.esa.int/p2sa/#ftp
[18] C. Geuzaine and J.-F. Remacle, "Gmsh: A 3-D finite element mesh generator with built-in pre-and post-processing facilities," *Int. J. Numer. Methods Eng.*, vol. 79, no. 11, pp. 1309–1331, Sep. 2009.
[19] R. Marchand, "PTetra, a tool to simulate low orbit satellite–plasma interaction," *IEEE Trans. Plasma Sci.*, vol. 40, no. 2, pp. 217–229, Feb. 2012.
[20] N. Imtiaz and R. Marchand, "Particle-in-cell modeling of dual segmented Langmuir probe on PROBA2," *Astrophys. Space Sci.*, vol. 360, no. 1, pp. 1–8, Nov. 2015.
[21] R. Marchand and P. A. Resendiz Lira, "Kinetic simulation of spacecraft–environment interaction," *IEEE Trans. Plasma Sci.*, vol. 45, no. 4, pp. 535–554, Apr. 2017.
[22] R. Marchand, "Test-particle simulation of space plasmas," *Commun. Comput. Phys.*, vol. 8, no. 3, pp. 471–483, 2010.
[23] F. Mackay, R. Marchand, K. Kabin, and J. Y. Lu, "Test kinetic modelling of collisionless perpendicular shocks," *J. Plasma Phys.*, vol. 74, no. 3, pp. 301–318, Jun. 2008.
[24] R. Marchand, F. Mackay, J. Lu, and K. Kabin, "Consistency check of a global MHD simulation using the test-kinetic approach," *Plasma Phys. Controlled Fusion*, vol. 50, no. 7, 2008, Art. no. 074007.
[25] G. Voitcu, M. Echim, and R. Marchand, "Comparative study of forward and backward test-kinetic simulation approaches," *Comput. Phys. Commun.*, vol. 183, no. 12, pp. 2561–2569, Dec. 2012.
[26] A. R. H. Heryudono and T. A. Driscoll, "Radial basis function interpolation on irregular domain through conformal transplantation," *J. Sci. Comput.*, vol. 44, no. 3, pp. 286–300, 2010.
[27] T. A. Driscoll and A. R. H. Heryudono, "Adaptive residual subsampling methods for radial basis function interpolation and collocation problems," *Comput. Math. Appl.*, vol. 53, no. 6, pp. 927–939, Mar. 2007.
[28] Q. Zhang, Y. Zhao, and J. Levesley, "Adaptive radial basis function interpolation using an error indicator," *Numer. Algorithms*, vol. 76, no. 2, pp. 441–471, Oct. 2017.
[29] A. Olowookere and R. Marchand, "Fixed bias probe measurement of a satellite floating potential," *IEEE Trans. Plasma Sci.*, vol. 49, no. 2, pp. 862–870, Feb. 2021.
[30] G. Liu and R. Marchand, "Inference of m-NLP data using radial basis function regression with center-evolving algorithm," *Comput. Phys. Commun.*, vol. 280, 2022, Art. no. 108497, doi: 10.1016/j.cpc.2022.108497.
[31] B. K. Spears *et al.*, "Deep learning: A guide for practitioners in the physical sciences," *Phys. Plasmas*, vol. 25, no. 8, Aug. 2018, Art. no. 080901.
[32] Y. R. Park, T. J. Murray, and C. Chen, "Predicting sun spots using a layered perceptron neural network," *IEEE Trans. Neural Netw.*, vol. 7, no. 2, pp. 501–505, Mar. 1996.
[33] N. A. Barkhatov and S. E. Revunov, "Neural network classification of discontinuities in space plasma parameters," *Geomagnetism Aeronomy*, vol. 50, no. 7, pp. 894–904, Dec. 2010.
[34] H. Chen, V. Chandrasekar, H. Tan, and R. Cifelli, "Rainfall estimation from ground radar and TRMM precipitation radar using hybrid deep neural networks," *Geophys. Res. Lett.*, vol. 46, nos. 17–18, pp. 10669–10678, Sep. 2019.
[35] C. M. Bishop *et al.*, *Neural Networks for Pattern Recognition*. London, U.K.: Oxford Univ. Press, 1995.
[36] T. Bazzi, R. Ismail, and M. Zohdy, "Comparative performance of several recent supervised learning algorithms," *Learning*, vol. 1, no. 1, p. 1, 2018.
[37] J. Zhang, "Gradient descent based optimization algorithms for deep learning models training," 2019, *arXiv:1903.03614*.
[38] P. Goldsborough, "A tour of tensorflow," 2016, *arXiv:1610.01178*.
[39] D. P. Kingma and J. Ba, "Adam: A method for stochastic optimization," 2014, *arXiv:1412.6980*.
[40] S. Santandrea *et al.*, "PROBA2: Mission and spacecraft overview," *Sol. Phys.*, vol. 286, no. 1, pp. 5–19, Aug. 2013.

Akinola Olowookere is currently pursuing the Ph.D. degree with the Department of Physics, University of Alberta, Edmonton, AB, Canada.

His current research interests include satellite interaction with space environment, application of machine learning, and artificial intelligence to space physics.

Richard Marchand is currently a Professor of physics with the University of Alberta, Edmonton, AB, Canada, where he does research on computational physics, space physics, and spacecraft–environment interaction.